Forecasting seismicity rate in the north-west Himalaya using rate and state dependent friction law

Prasanta Chingtham, Sanjay K. Prajapati, Vineet K. Gahalaut, Sumer Chopra & Pareshnath Singha Roy

Taylor & Francis
Taylor & Francis Group

Forecasting seismicity rate in the north-west Himalaya using rate and state dependent friction law

Prasanta Chingtham[a], Sanjay K. Prajapati[a], Vineet K. Gahalaut[a], Sumer Chopra[b] and Pareshnath Singha Roy[c]

[a]National Center for Seismology, Ministry of Earth Sciences, New Delhi, India; [b]Institute of Seismological Research, Gandhinagar, India; [c]Indian Institute of Technology (Indian School of Mines), Dhanbad, India

ABSTRACT

In this study, rate and state Coulomb stress transfer model is adopted to forecast the seismicity rate of earthquakes ($M_W \geq 5$) in the north-west Himalaya region within the testing period 2011–2013. Coulomb stress changes (ΔCFF), considered to be the most critical parameter in the model, exhibit stress increase in the whole study region, excluding the Chaman fault of the Kirthar range where significant stress shadow has been observed. The estimated background seismicity rate varies in the range 0.0–0.7 in the region, which is preoccupied by low aftershock duration of <50 years. Furthermore, a low b-value that varies between 0.54 and 0.83 is observed in Kirthar ranges, Karakoram fault and Pamir-Hindukush region. However, areas like Hazara syntaxis of the northern Pakistan and northern Pamir of the Eurasian plate exhibit higher b-values in the range 1.23–1.74. Considering constant constitutive properties of the faults (i.e. $A\sigma$ = 0.05 MPa), our forecast model for variable ΔCFF and heterogeneous b-value successfully captures the observed seismicity rate of earthquakes. Results have been verified using statistical S-test. However, the model fails to capture the observed seismicity rate during the period when reconstructed for average b-value to be 0.86 and no change in ΔCFF (ΔCFF = 0).

1. Introduction

In last few decades, studies and interests in earthquake forecasting have increased tremendously. The rate and state friction law, as introduced by Dieterich (1979, 1994) on the basis of laboratory friction experiments, has been frequently used to model seismic activity. The model can be categorized into aseismic or seismic (earthquakes) based on chosen parameters (physical constitutive properties of faults, the stressing rate, and the background seismicity rate) incorporated into this rate and state friction law (Helmstetter and Shaw 2006). In unstable condition, the rate and state law provides a relation between stress history and seismicity (Dieterich 1994).Therefore, this model can be used to forecast seismicity rate changes caused by Coulomb stress changes (ΔCFF) after the mainshocks. Moreover, several recent studies have discussed this model and applied it in different seismically active regions for understanding the temporal and spatial response of seismicity due to successive stress changes, including, toggling, decay, and aftershock migration for seismic hazard assessment (King et al. 1994; Nalbant et al. 1998; Stein 1999, 2003).

CONTACT Sanjay K. Prajapati go2sanjay_p@yahoo.com

Supplemental data for this article can be accessed at https://doi.org/10.1080/19475705.2017.1369168.

Several worldwide evidences have been reported that the small changes in ΔCFF in rate and state Coulomb stress transfer model can enhance the seismicity rate in areas of high background seismicity and can also suppress the same in areas of stress shadows with previously high seismicity rates (Steacy et al. 2005). Parsons (2002) has also successfully demonstrated that the highest probability rate for triggered seismicity is associated with the ΔCFF after the mainshocks, corroborating the model proposed by Dieterich (1994). Gomberg et al. (2000, 2005) also elucidated the model's ability in explaining the temporal behaviour of seismicity and in justifying the variation of time delays between successive events. Several investigators have considered the ΔCFF and background seismicity rate (r) for investigating seismicity, earthquake migration and seismic hazard assessment (Mccloskey et al. 2005; Nalbant et al. 2005). Toda et al. (2005) calculated the expected seismicity rate of next ten years in southern California. Further, Toda and Enescu (2011) modified the methodology which was previously adopted by several authors (Hainzl et al. 2009; Toda et al. 2005) for forecasting $M_W \geq 5$ shallow crustal earthquakes for Japan's mainland.

The seismically active north-west (NW) Himalayan region is formed due to oblique compression between the Indian and Eurasian plates, thereby resulting in large scale thrusting and rotation of faulted blocks (Valdiya 1991). The folds and thrust belts that exist in the study region are also considered to be seismically most active zones in the world (Khwaja and Monalisa 2005) (Figure 1). The seismological investigation of the area reveals that the occurrence of earthquakes ($M_W \geq 4$) is closely associated with both the surface and blind faults (Khwaja and Monalisa 2005). Seismic hazard evaluation in this seismically active Himalaya is therefore important because earthquakes cause several types of threats to the people living adjacent to this gigantic mountain chain. In addition, it is widely believed that numerous active faults in the geological past have potential and may be
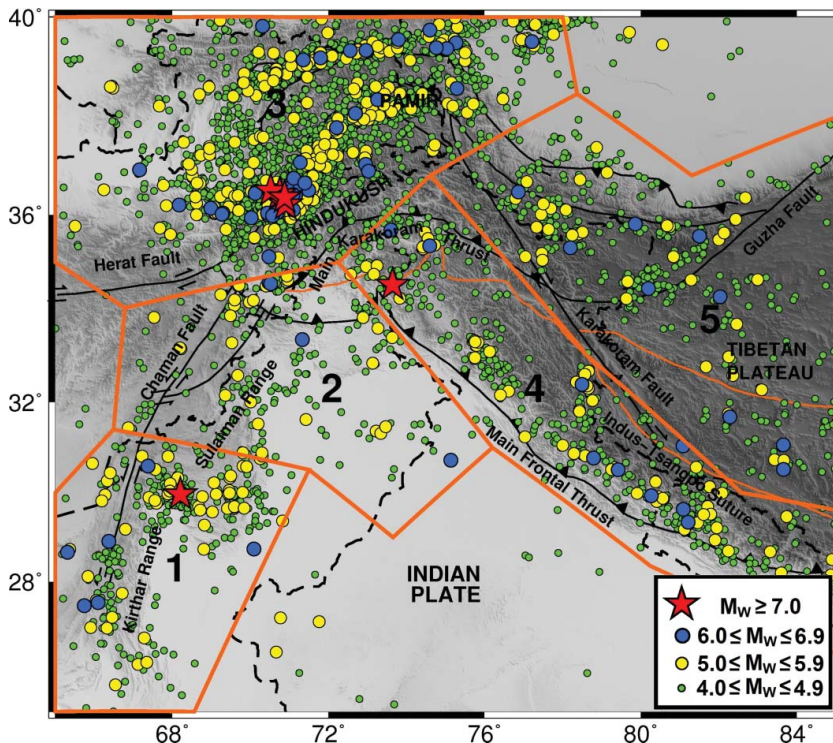
Figure 1. A seismotectonic map of the study region prepared with the epicentral distribution of independent earthquakes (mainshocks) of $M_W \geq 4$ occurred during the period 1975–2010. Major fault systems of the NW Himalaya are shown by black line. Dashed lines indicate the political boundary. Red lines indicate five broad seismogenic source zones on the basis of seismicity, tectonics and focal mechanism of earthquakes as suggested by Yadav et al. (2011). All zones are indicating by number i.e. 1, 2, 3, 4 and 5. (To view this figure in colour, see the online version of the journal).

reactivated in future (Philip et al. 2014). They also elucidated that these active faults may trigger seismic activity (>80% seismic activity) in the study region.

In present study, we forecast the seismicity rate during the period 2011–2013 in the NW Himalaya and its adjoining region using modified rate and state model as proposed by Toda and Enescu (2011). We also determine the probability of $M_W \geq 5.0$ shallow crustal mainshock occurrences using homogenized M_W earthquake catalogue from International Seismological Centre (ISC) and Global Centroid moment tensor (GCMT) accessible at http://www.isc.ac.uk/bulland http://www.globalcmt. org/CMTsearch.html, respectively, in the five broad seismogenic zones of NW Himalaya and its surrounding regions. These broad source zones have been delineated by Yadav et al. (2012) by considering the information of historical and instrumental seismicity, tectonics, geology, paleoseismology and other neo-tectonic properties of the studied region (Tandon and Srivastava 1974; Chandra 1978; Bapat et al. 1983; Oldham 1883). The present forecasting study is commonly known as pseudo-prospective testing and the forecasting model largely considers the constrained input parameters, based on the physical mechanism of earthquake occurrences, for estimating seismicity rates for the region in the testing period (Cocco et al. 2010; Strader and Jackson 2015).

2. Earthquake catalogue and fault plane solution

It is well accepted that going back in time leads to lower quality and inadequacy of data in comparison with the more recently obtained ones (Leptokaropoulos et al. 2012). Hence, we have analysed seismicity data between 1975 and 2010 from the earthquake catalogues of ISC and GCMT for forecasting the seismicity rate using rate and state friction law. On the basis of recording wave types of earthquakes, the catalogues comprise of different magnitude scales, i.e., local magnitude (M_L), body wave magnitude (m_b), surface wave magnitude (M_S) and moment magnitude M_W. However, the magnitude scales such as M_L, m_b and M_S saturate at different higher magnitudes and therefore need to be converted into a single non-saturated magnitude scale for avoiding incorrect estimation of any statistical analyses (Chingtham et al. 2014). For this purpose, a homogenized earthquake catalogue in M_W is compiled from ISC and GCMT databases, for the period 1975–2010, by utilizing the regression technique as adopted by Yadav et al. (2011) for the study region bounded by latitude, 25°N - 40°N and longitude, 65°E - 85°E (Figure 2(a)). The spatial and temporal windowing method of Knopoff (2000) is employed for declustering the catalogue (Figure 2(b)). We have also checked the completeness of magnitude (M_C) for each sub-region by fitting the power law to the frequency magnitude distribution of earthquakes at 90% confidence level (Figure 3(a)–(e)) Here, the Maximum Curvature method is adopted for estimating M_C in each source zone. The calculated M_C for source zones 1, 2, 3, 4 and 5 are found to be 4.1, 4.3, 4.0, 4.0 and 4.3, respectively. During the period 1975–2010, the annual rates of declustered seismicity are then calculated in the square cells of 0.5° × 0.5° by considering only the earthquake magnitudes above the minimum magnitude in each source region. Then Gaussian function of Frankel (1995) with correlation distance of 100 km is applied to smooth the annual rates of declustered seismicity. For our forecasting purpose, 20% of the minimum rate is assigned to the particular cells having zero seismicity rates. Furthermore, we obtained the focal mechanism solution from GCMT catalogue for computing the ΔCFF. The key problem for computing ΔCFF computation is precisely defined by receiver's fault mechanisms in each source zone. In present study, we computed coulomb stress changes based on specified fault for each zone except Zone 3. For Zone 3, we assumed the multiple receiver fault orientations as suggested by Hainzl et al. (2010) and Steacy et al. (2005). Details of the earthquake sources used in the analyses for the study region are mentioned in Table 1.

3. Methodologies

3.1. Seismic sources

We consider mainshocks of magnitude $M_W \geq 5$ that occurred after 1975 as the seismic sources for computing ΔCFF (Figure 4). Some moderate to large earthquakes that occurred in this study region
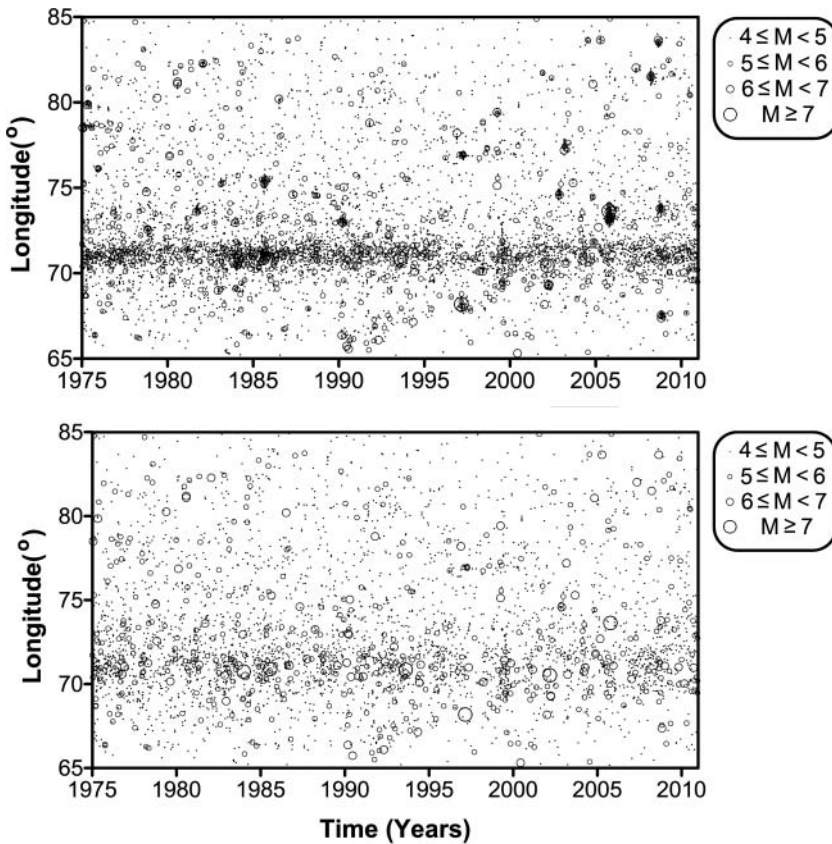
Figure 2. Comparison between the observed and declustered earthquake catalogues ($M_W \geq 4.0$). (a) Time-longitude plot of seismicity using ISC catalogue. (b) Time-longitude plot for the earthquake catalogue declustered using the Knopoff (2000) algorithm.

are listed in Table 1. A variable slip model has been used for 8 October 2005 Kashmir earthquake, while a simple uniform slip model obtained from the established empirical relations of Wells and Coppersmith (1994) is considered for other earthquakes for estimating ΔCFF.

3.2. Receiver faults

The basic information on the fault geometry and slip direction of the receiver faults is essential and necessary for computing ΔCFF. Two different approaches are primarily adopted while taking into account the types of receiver faults for estimating ΔCFF (King et al. 1994; Toda and Enescu 2011). The first approach commonly known as specified fault considers that the regional dominant faulting mechanisms of the receiver source faults have similar focal mechanisms with those of the mainshock source faults due to the complex fault systems (Nostro et al. 2005). The other approach comprises of resolving the optimally oriented planes for Coulomb failure (King et al. 1994; King and Cocco 2001), and thereby considering the maximized total stress tensor obtained from the optimized values of strike, dip and rake of the source faults (Toda et al. 2005). As such, the predicted focal mechanisms associated with optimally oriented planes strongly depend on the orientation and magnitude of the regional stress fields.

In this study, the specified fault approach is adopted because the regional stress tensor is not well described for the study region. The Main Himalayan Thrust (MHT), Karakoram fault and Chaman fault (CF) are some of the major regional active faults and geological structures that control the
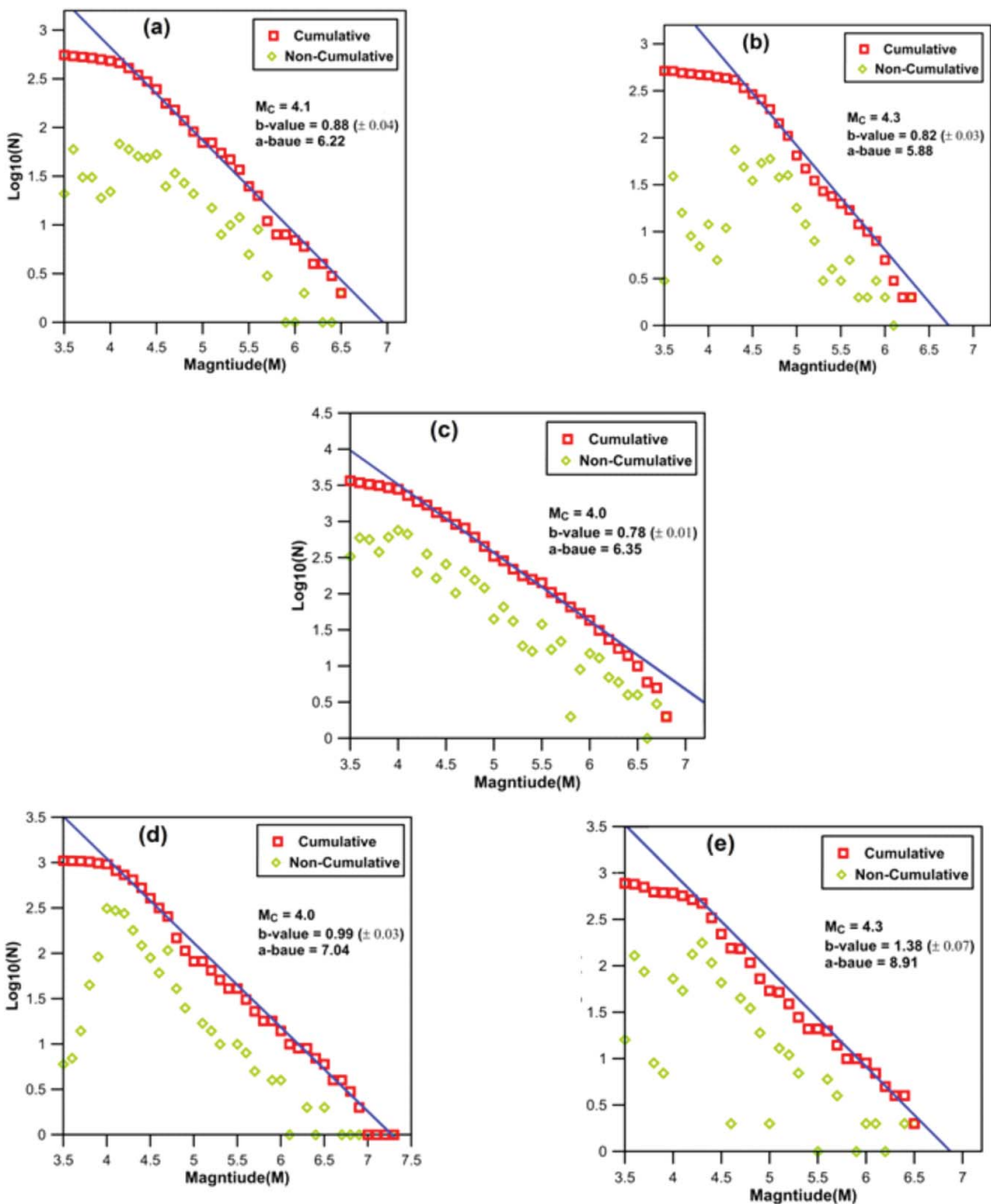
Figure 3. Frequency magnitude distribution plot in all the five zones [(a)–(e)] of the NW Himalaya and its adjoining regions estimated by fitting the power law at 90% confidence level. (To view this figure in colour, see the online version of the journal).

seismotectonics of the study region. Central Himalayan region is well dominated by thrust faults with low dip angles (Shanker et al. 2011) whereas Pamir-Hindukush region exhibits reverse as well as strike-slip faults with active structures (Fan et al. 1994; Shanker et al. 2011). Mixtures of both the normal and right lateral strike-slip faulting earthquakes and also active geological structures are quite prevalent in the Karakoram Himalaya (Figure 5(a)). Both the focal mechanisms and active fault information are utilized to select dominant regional mechanisms for each zone and subsequently, the grid map of these typical focal mechanisms at every 0.5° interval is plotted by

Table 1. List of earthquakes larger than magnitudes $M_W \geq 6.0$ that occurred during the period 1975–2010, and their considered source parameters for calculating coseismic ΔCFF.

| Year	Latitude (°)	Longitude (°)	M_W	Depth (km)	Nodal plane 1 Strike (°)	Dip (°)	Rake (°)	Nodal plane 2 Strike (°)	Dip (°)	Rake (°)	Length (km)	Width (km)	Estimated slip (m)	Fault model
31 January 1977	39.85	69.79	6.0	10.0	296	35	99	104	55	83	12	7	0.55	Empirical
16 March 1978	29.83	66.43	6.1	39.2	197	13	116	351	78	84	14	8	0.46	Empirical
1 November 1978	39.34	72.16	6.6	39.34	103	58	163	202	75	33	31	14	0.78	Empirical
29 July 1980	29.42	80.95	6.5	22.3	290	21	91	108	69	89	26	12	0.70	Empirical
12 September 1981	35.22	73.48	6.1	35.22	107	36	79	300	54	98	14	8	0.45	Empirical
23 January 1982	31.71	82.24	6.3	10.0	17	38	−58	160	59	−112	20	10	0.52	Empirical
16 December 1982	36.20	68.71	6.4	12	218	43	113	9	51	70	23	11	0.64	Empirical
13 February 1983	39.94	75.11	6.2	15	230	60	−7	323	84	−149	17	9	0.483	Empirical
30 December 1983	37.17	70.41	7.4	37.17	273	18	81	103	72	93	105	30	1.5	Empirical
1 February 1984	34.19	70.05	6.1	15	268	37	121	50	59	69	15	8	0.46	Empirical
26 October 1984	38.99	71.03	6.1	38.99	37	77	9	305	81	167	15	8	0.46	Empirical
23 August 1985	39.54	75.09	6.9	15.4	315	29	159	63	80	62	50	19	0.87	Empirical
11 September 1985	39.50	75.32	6.1	10	90	44	68	299	50	110	15	8	0.47	Empirical
4 March 1990	28.66	66.16	6.0	28	278	78	−176	187	86	−12	12	7	0.44	Empirical
5 March 1990	37.04	72.85	6.1	17.5	192	36	−46	322	65	−117	15	8	0.42	Empirical
17 June 1990	26.75	65.25	6.1	15	210	63	15	114	77	153	15	8	0.45	Empirical
19 October 1991	30.22	78.24	6.8	15	317	14	115	112	78	84	35	17	0.98	Empirical
20 May 1992	32.95	71.27	6.0	15	237	5	79	68	85	91	12	7	0.45	Empirical
1 May 1994	37.10	66.85	6.1	24	105	47	120	245	51	62	14	8	0.51	Empirical
19 March 1996	39.93	76.8	6.3	22.2	273	26	109	72	66	81	20	10	0.62	Empirical
19 November 1996	35.45	77.86	6.8	15	180	71	170	273	81	19	40	16	0.93	Empirical
27 February 1997	29.74	68.13	7.1	15.3	298	15	122	85	77	82	67	23	1.07	Empirical
11 April 1997	39.61	76.93	6.1	15	240	37	−45	9	65	−118	14	8	0.47	Empirical
30 May 1998	37.38	70.08	6.5	24.1	200	79	−7	291	83	−169	26	12	0.66	Empirical
27 August 1998	39.51	77.22	6.3	15	240	78	0	330	90	−168	20	10	0.52	Empirical
28 March 1999	30.38	79.21	6.5	15	280	7	75	115	83	92	26	12	0.67	Empirical
25 March 2002	36.28	69.06	6.1	15	16	39	104	177	53	79	14	8	0.47	Empirical
20 November 2002	35.52	74.66	6.3	15	204	30	−117	55	64	−75	20	9	0.51	Empirical
24 February 2003	39.37	77.24	6.3	24	239	33	62	92	61	107	20	10	0.55	Empirical
11 July 2004	30.56	83.78	6.2	13	359	45	−74	156	47	−106	17	9	0.48	Empirical
7 April 2005	30.24	83.77	6.3	12	170	43	−91	351	47	−89	20	10	0.53	Empirical
8 October 2005	34.38	73.47	7.6	15.7	321	31.5	123	114	57	65	100	30	6.0	Parsons et al. (2006)
8 October 2005	34.70	73.12	6.4	12	328	39	107	127	53	77	22	10	0.61	Empirical
8 January 2007	39.85	70.17	6.0	22.8	187	65	13	91	78	155	12	7	0.42	Empirical
5 May 2007	34.33	81.97	6.1	23.9	220	88	2	130	88	178	14	8	0.47	Empirical
20 March 2008	35.43	81.37	7.1	12	358	41	−110	203	52	−74	66	22	1.10	Empirical
25 August 2008	30.61	83.51	6.7	17.3	30	48	−48	157	56	−127	36	15	0.76	Empirical
25 September 2008	30.66	83.69	6.0	21.2	208	75	−13	302	77	−165	12	7	0.41	Empirical
5 October 2008	39.5	73.64	6.7	12	246	38	78	82	53	99	30	15	0.78	Empirical
28 October 2008	30.4	67.48	6.4	12	304	73	171	37	81	18	22	11	0.62	Empirical
29 October 2008	30.29	67.57	6.4	12	324	68	−178	233	88	−22	22	11	0.61	Empirical
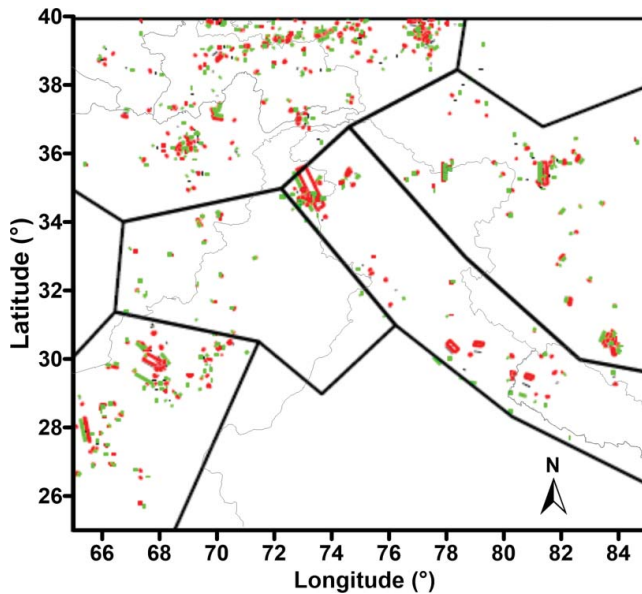
Figure 4. Earthquake sources used for calculating the Coulomb stress changes (ΔCFF) since 1975. Most of the earthquakes are modelled by using a simple uniform slip model obtained from the empirical relations of Wells and Coppersmith (1994) except the 2005 Kashmir earthquake where variable slip distributions is used (Parsons et al. 2006). Red lines denote active faults of each source zone and green lines indicate the surface projection of the faults. (To view this figure in colour, see the online version of the journal).

smoothing out based on the available method of Terakawa and Matsu'ura (2008) (Figure 5(b)). In Figure 5(b), Zone 4, we observed the normal faulting with varying direction along with dominated large thrust fault system. Such spatial distribution of faulting is also mirrored by GPS data (Hintersberger et al., 2010). The normal faults in Zone 4 are neither limited to higher Himalaya nor they associate with larger regional scale structure. Normal faults are closely spaced and have pervasively affected the rocks of the thrust belt (Hintersberger et al., 2010). Hintersberger et al. (2010) suggest
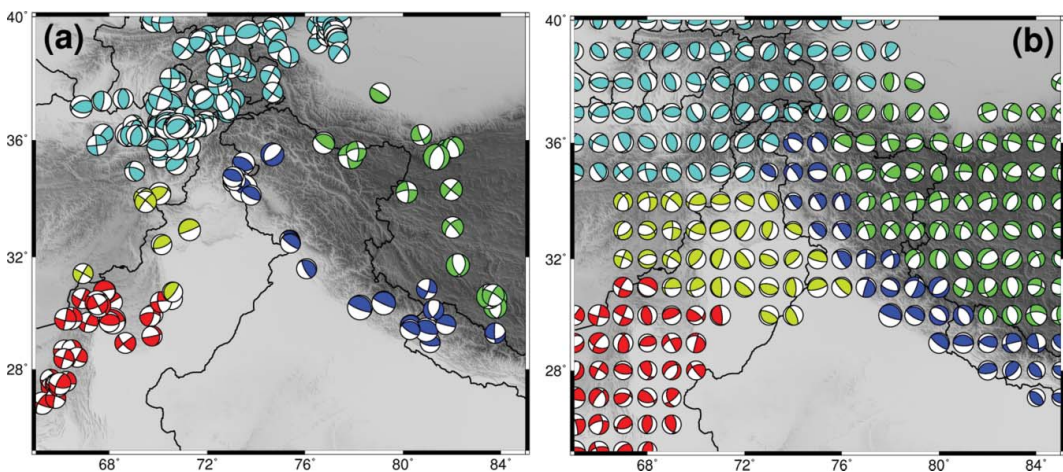

Figure 5. (a) Well-determined focal mechanisms for $M_W \geq 5$ earthquakes shown by different colours, with each colour depicting different source zones as mentioned in Figure 1(b) Smoothed faulting mechanisms taking the information of earthquake focal mechanism and active fault into consideration at every $0.5° \times 0.5°$ grid for selecting dominant regional mechanisms for each zone and consider as one homogeneous source for computing ΔCFF. (To view this figure in colour, see the online version of the journal).

that reverse faults generated during NE–SW shortening were reactivated as normal faults during NE-SW extension. Such NE-SW extension in the upper crust seems to be related to ramp−like geometry of the underthrusting zone along the MHT and the motion of Himalayan rocks over such ramp as suggested by Hintersberger et al., 2010. Furthermore, Negi et al. (2017) has suggested that the weak evidence of normal fault mechanism at shallow depth is non-seismogenic feature with no persistent record at depth. Therefore in present forecast modelling we did not consider the fault mechanism other than regional fault mechanism for Zone 4.

3.3. Coulomb stress changes and its associated parameters

In an elastic half-space, the static Coulomb stress changes (ΔCFF) caused by each mainshock (Okada 1992) is calculated by considering 0.25 and 32 GPa as Poisson's ratio and shear modulus respectively. The simplifying assumptions of pore pressure effects (King et al. 1994) are primarily taken into account to compute ΔCFF by using the following equation:

$$\Delta CFF = \Delta\tau + \mu' \Delta\sigma_n \tag{1}$$

where $\Delta\tau$ is the shear stress in the direction of slip on the assumed causative fault plane. $\Delta\sigma_n$ is the normal stress changes (positive for unclamping or extension) and μ' is the effective coefficient of friction for all the fault.

We have used uniform slip model for computing ΔCFF for all the events except 8 October 2005 Kashmir earthquake, where finite slip model is given by Parsons et al. (2006). Then the maximum ΔCFF has been computed from the seismogenic depth range for each zone i.e., for Zone 1, 0–15 km, Zone 2, 0–15 km, Zone 3, 0–35 km, Zone 4, 0–15 km, and Zone 5, 0–20 km (depth range for each zone is detailed in Supplementary Figure S1). As discussed earlier, ΔCFF for each zone is computed on specified fault except for Zone 3 where the characteristics of the mainshock occurrences are totally different due to complex fault systems. Figure 6 depicts that the study area is mostly dominated with high ΔCFF, except at few patches in Zone 1 and Zone 5 with low ΔCFF.

As we assumed the uniform slip model to compute the ΔCFF, sensitivity analysis assuming the uniform slip model with 10%, 20% and 30% variable in slip has been done to test the sensitivity of
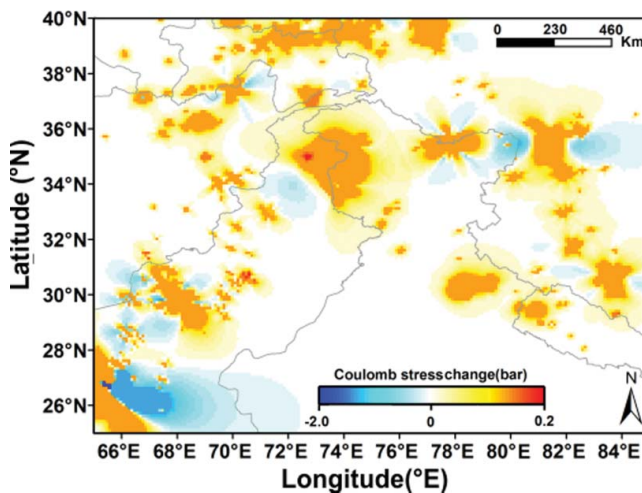

Figure 6. Static Coulomb stress changes (ΔCFF) associated with $M_W \geq$ 5.0 earthquakes that occurred in study area since 1975 and incorporated in modeling. Both nodal planes are considered for resolving stresses within the seismogenic depth of 5–15 km. Here maximum ΔCFF value is chosen and plotted for estimating the stress perturbations. (To view this figure in colour, see the online version of the journal).

ΔCFF (Supplementary Figure S2). We have also compared our results with available slip model for Kashmir earthquake (Parsons et al. 2006) independently; variations in ΔCFF are shown in Figure S2. In case of the uniform slip model, despite of changing the slip amount, the overall stress patterns are found to be consistent. Parsons et al. (2006) have done similar test for 2005 Kashmir earthquake with changing friction coefficient and target fault depth, and found the overall stress change pattern to be consistent.

3.4. Background seismicity rate

A fair understanding of r is a prerequisite for studying the effects of ΔCFF on the seismicity of a region. Although, the definition and the measure of r is still controversial (Hainzl and Ogata 2005; Lombardi et al. 2006; Lombardi and Marzocchi 2007), there are two different approaches generally reported in several literatures for retrospective seismicity forecasting (Toda and Enescu 2011). Toda et al. (2005) defined the first approach as the seismicity rate r before the occurrence of large earthquakes while the other approach considers r as a time independent smoothed seismicity rate estimated from the declustered catalogue in a prescribed time window (Catalli et al. 2008). In this paper, the approach provided by Catalli et al (2008) is used to estimate r from the declustered catalogue as shown in Figure 7.

3.5. Time-dependent rate and state formulation

Seismicity of a region for a particular time period can be examined through the history of stress perturbations and its corresponding state variable and seismicity rate changes associated with multiple mainshocks. The spatial heterogeneities of ΔCFF at each node of grids is estimated for every moderate to large mainshocks. The seismicity rate R of a region is related to the tectonic secular shear stressing rate, $\dot{\tau}$, and the state variable, γ, (Dieterich 1994) by the following equation:

$$R = \frac{r}{\dot{\gamma}\tau} \tag{2}$$

where r is the background seismicity rate of the considered area and γ is the state variable that evolves with time and stressing history. For a constant $\dot{\tau}$, γ at each node takes the value given by the
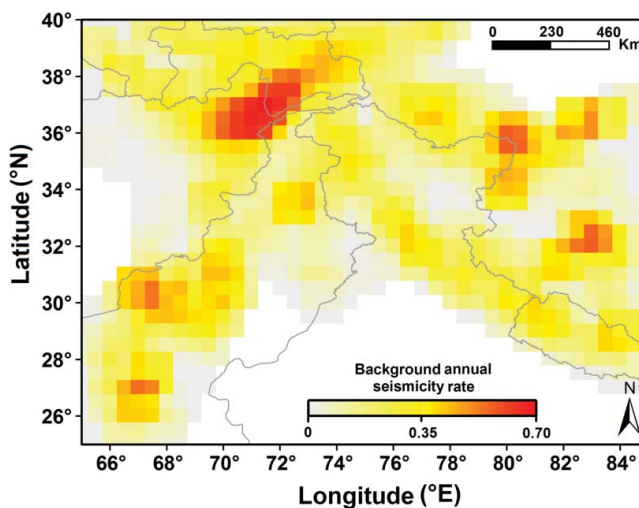

Figure 7. Background seismicity rate in the study area based on the declustered ISC catalogue of 35 years (1975–2010). The observed background seismicity rate is used for forecasting the seismicity. (To view this figure in colour, see the online version of the journal).

following equation:

$$\gamma_o = \frac{1}{\dot{\tau}}$$ (3)

which accordingly gives $R = r$. This implies that the seismicity rate is the background seismicity rate without the presence of stress perturbation. Therefore, the initial γ_o changes to a new γ due to increased/decreased ΔCFF after the mainshocks, following the equation:

$$\gamma_n = \gamma_{n-1} \exp\left(\frac{-\Delta CFF}{A\sigma}\right)$$ (4)

where γ_{n-1} and γ_n are the values of the state variable just before and after the applied ΔCFF, respectively. The product, $A\sigma$ is an important controlling parameter for fault friction and here its value is taken to be 0.05 MPa (Toda and Stein 2003). Hence, seismicity can be easily obtained by substituting this new state variable in Equation (4) during the time of stress perturbations. An increased ΔCFF on a fault finally increases the seismicity rate by producing large slip due to decreased γ while a sudden stress drop increases γ and lowers the seismicity rate (Toda and Enescu 2011). Then, γ can be approximated for any next time step Δt by using the relation:

$$\gamma_{n+1} = \left[\gamma_n - \frac{1}{\dot{\tau}}\right] \exp\left(\frac{-\Delta t \dot{\tau}}{A\sigma}\right) + \frac{1}{\dot{\tau}}$$ (5)

In rate- and -state dependent friction model, aftershock duration, t_a, can be expressed with $A\sigma$ and $\dot{\tau}$ (Dieterich 1994) through the given equation:

$$t_a = \frac{A\sigma}{\dot{\tau}}$$ (6)

where t_a is the duration of transient effects or the aftershock duration that defines the characteristic time for aftershocks to return to the background seismicity rate.

Toda and Enescu (2011) suggested that the stress release takes several time periods (e.g. decades to centuries), mostly on the inactive faults. Along the plate interface, the stressing rate is found maximum but diminishes from the interface as a function of time. As such, the duration of such observed t_a of the collision/subduction event is found to be much smaller in comparison to the mainshocks located in the stable continent. The stressing rate for a constant $A\sigma$ taken throughout time and space in the Dieterich model is found to be inversely proportion to t_a(equation 4). By considering the plate interface's distance and spatially clustered aftershock distributions of earlier large earthquakes, the spatially variable t_a is arbitrarily assigned to each node of the grids (Figure 8). Thus, it is practically observed that the spatial distribution of t_a strongly influences the initial condition of γ. We start our calculations by assuming spatially non- homogeneous steady state variable (γ_o) as the collision region generally exhibits lower γ, whereas high γ is mostly observed in the stable region. Furthermore, ΔCFF at discrete time step is computed that involves γ changing with respect to time and space (equations (4) and (5)).

3.6. b-*value calculation and extrapolation of large earthquakes*

A maximum likelihood procedure (Aki 1965) is adopted to compute *b*-value at each node from at least 50 events encapsulated by $0.5° \times 0.5°$ grid. However, the *b*-value was not calculated due to incompleteness issue for those nodes where the total number of earthquakes having magnitudes greater than or equal to M_C was less than 25. Hence, the estimation process tends to introduce
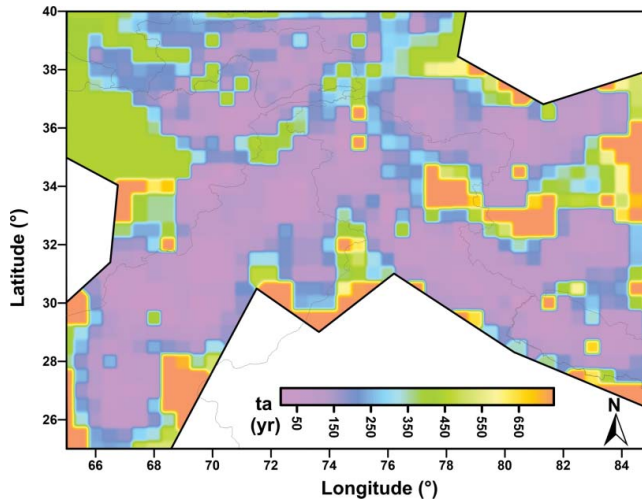
Figure 8. Aftershock duration (t_a) estimated from the stressing rate ($\dot{\tau}$) for all zones. (To view this figure in colour, see the online version of the journal).
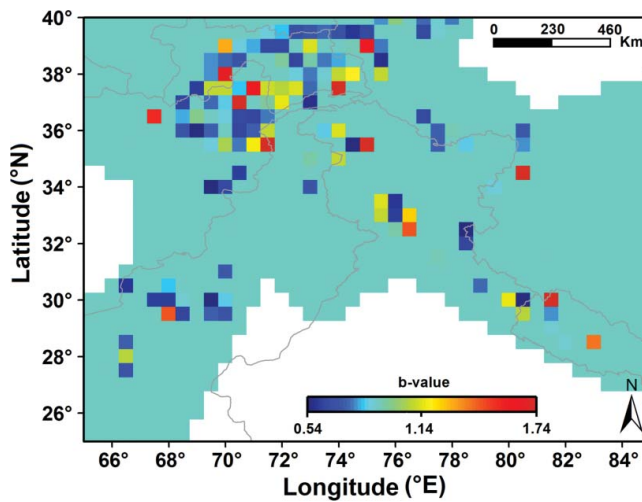

Figure 9. Spatial distribution of b-value estimated by using the maximum likelihood method. Here, an average b-value of 0.86 is arbitrarily assigned to those nodes where the b-value was not calculated due to incompleteness issues for forecasting purpose. (To view this figure in colour, see the online version of the journal).

spatial gaps due to constraints on the estimation of parameters by the number of earthquakes (Chingtham et al. 2014; Thingbaijam et al. 2008, 2009). In such cases, an average b-value is arbitrarily assigned to those particular nodes for forecasting purpose. Finally, the constant b-value estimation at each node is utilized for extrapolating the occurrence rate of small earthquakes to large earthquakes as suggested by Toda and Enescu (2011) (Figure 9).

3.7. Spatial likelihood test (S-test)

Statistical testing of earthquake forecast is an important task for introspecting the consistency of the forecast model and for this several procedures/methodologies exist. Kagan and Jackson (1995)

introduced three different tests namely the number test (N-test), the likelihood test (L-test), and the ratio test (R-test) to quantify the earthquake predictability for improving the seismic hazard estimation. In our present analysis, we tested our forecast model by using the spatial likelihood test, i.e. S-test as shown in Figure 12.

In this test, the spatial information is firstly extracted by summing the forecasted expected rates over the magnitude bins and later normalized its sum so that the sum gives the total number of observed earthquakes. Following the common notations used by Zechar et al. (2010), we can define the expected rates and the observed earthquakes as given below:

$$\Omega^s = \{w^s(j) \mid j \in S\} \qquad w^s(j) = \sum_{i \in M} w(i,j) \tag{7}$$

$$\Lambda^s = \{\lambda^s(j) \mid j \in S\} \, \lambda^s(j) = \frac{N_{\text{obs}}}{N_{\text{fore}}} \sum_{i \in M} \lambda(i,j) \tag{8}$$

where N_{obs} and N_{fore} indicates the total observed earthquakes and forecasted expected rates in the total magnitude-space bins, i.e. M and S defined in the study region. Here, $w(i,j)$ and $\lambda(i,j)$ also gives the number of earthquakes observed and forecasted expected rates in the particular magnitude–space bin (i,j). The observed joint log-likelihood which is estimated by considering these values is given by

$$S = L(\Omega^s \mid \Lambda^s) \tag{9}$$

In order to account for forecast uncertainty in the model, a set of simulated catalogues $(\hat{\Omega})$, is obtained by simulating 1000 times, where each catalogue can be represented as

$$\hat{\Omega}_x = \{\hat{\omega}_x(i,j) \mid (i,j) \in R\} \tag{10}$$

where $\hat{\omega}_x(i,j)$ gives the number of simulated earthquakes in bin (i, j). Then, the set $\{\hat{S}\}$ is constructed with the xth member equal to the joint log-likelihood of the xth simulated catalogue from each simulated catalogue and later compared with the observed joint log-likelihood. If this observed joint log-likelihood falls in the higher tail of simulated joint log-likelihood, then we can conclude that the observed and forecasted spatial seismicity patterns are consistent. However, this will not be true if we consider statistical S-test as a two-tailed test. In this study, we have considered S-test as one-tailed test by taking into consideration of those previous Collaboratory for the Study of Earthquake Prediction related studies (Schorlemmer et al. 2007; Zechar et al. 2010).

Finally, the quantile score ζ of S-test is estimated by using the following relation:

$$\zeta = \frac{|\{\hat{S}_x \mid \hat{S}_x \leq S\}|}{|\{\hat{S}\}|} \tag{11}$$

Where $\hat{S}_x$ is the observed joint log-likelihood. If the ζ value is very small then, we can say that the observed spatial distribution is found inconsistent with the forecast. However, more and more details about this test can be obtained from the literature of Zechar et al. (2010).

4. Results and discussion

In order to forecast the seismicity rate, the input model parameters have to be constrained a priori value based on the available data and information of the target study area. These input parameters are then incorporated into the modified rate and state model for forecasting the seismicity rate of earthquakes ($M_W \geq 5$) during the period 2011–2013 (Figure 10).
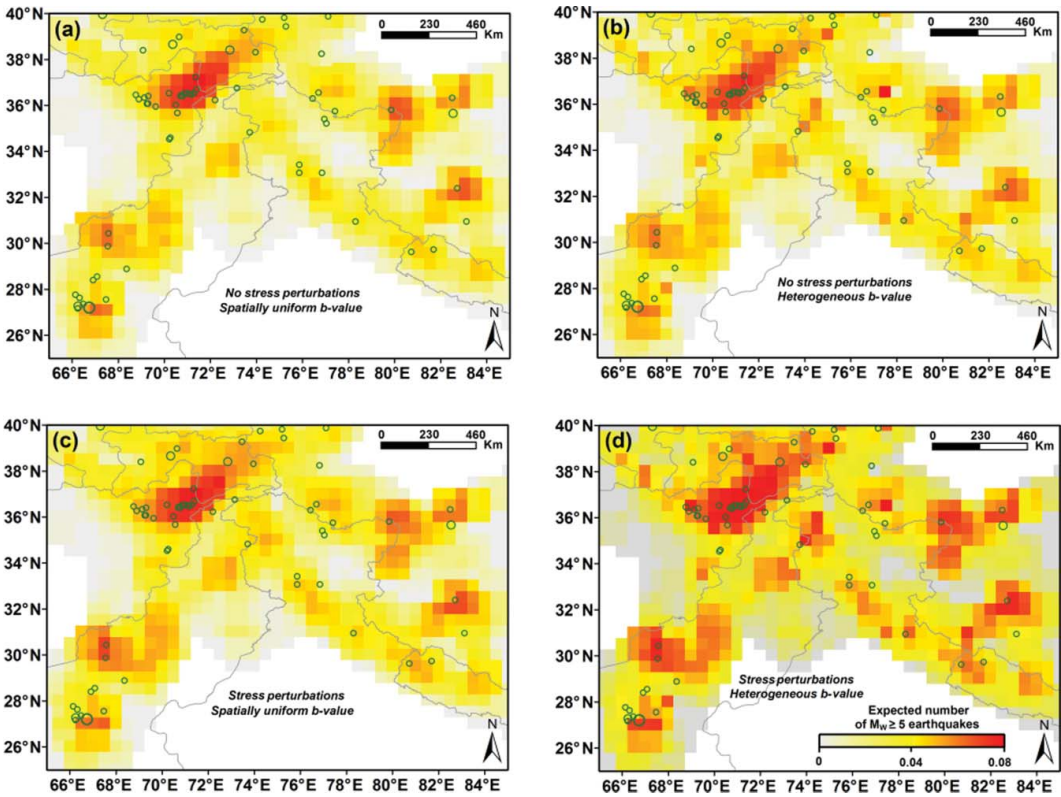
Figure 10. (a) Expected number of $M_W \geq 5$ earthquakes reproduced by reference model (i.e. ΔCFF = 0 and constant b-value (0.86)) along with the epicentral locations of the observed earthquakes during the period 2011–2013. (b) Expected number of $M_W \geq 5$ earthquakes calculated by ΔCFF = 0 and considering spatially variable b-value. (c) Expected number of $M_W \geq 5$ earthquakes reproduced by model with constant b-value (0.86). (d) Expected number of $M_W \geq 5$ earthquakes calculated by using spatially variable ΔCFF and b-value. (To view this figure in colour, see the online version of the journal).

4.1. Coulomb (ΔCFF) stress analysis

First, we compute ΔCFF for mainshocks ($M_W \geq 5$) at seismogenic depth based on specified fault approach (King et al. 1994). There are 41 $M_W \geq 5$ earthquakes spread over the entire zone that are listed in Table 1. Stress increase and/or decrease have been observed for significant earthquakes in the study region. The noticeable increase in ΔCFF are primarily associated with 17 June 1990 Pakistan earthquake (Zone 1), 19 October 1991 Uttarkashi earthquake, 28 March 1999 Chamoli earthquake and 8 October 2005 Kashmir earthquake (Zone 4). The 17 June 1990 strike-slip Pakistan earthquake may also have important contribution to the stress shadow observed in the Chaman fault (Kirthar Range). In Zone 5, most of the earthquakes that are of strike-slip and normal faulting type are responsible for deformation in the Tibetan plateau. Ogata (2005) showed that even small changes in ΔCFF i.e. increment/decrement can trigger respective activation/lowering of microseismicity. Toda et al. (2005) and Cocco et al. (2010) have also suggested that ΔCFF may not alone induce extraordinary seismic activity, but the combination of all other parameters, i.e. Aσ, the stressing rate and the background seismicity rate incorporating to the model, may result in significant triggering or rate decrease. Furthermore, Bhloscaidh et al. (2014) affirmed that the forecast ability of Coulomb-based models can also be considerably improved by employing spatial variations of r.

4.2. Seismicity rate changes

Considering the importance of r, we have calculated the spatial variations of annual background seismicity rate using declustered catalogue for the period 1975–2010. The value of r varies from 0-0.7 in the study region (Figure 7). The maximum seismicity rates are found in Zone 3 where the complex faults pattern and high seismicity is exhibited. The moderate background seismicity rate is found in Zones 1 and 5, where mostly strike-slip fault systems exist. In these zones, few large earthquakes have been documented in recent past (Table 1). Zone 2 is characterized by the diffused seismicity and moderate hazard. The high rate of seismicity in study region is primarily associated with the complex Himalayan thrust fault system formed during the continuous collision between the Indian and Eurasian plates (Avouac et al. 2001; Yadav et al. 2011)..

4.3. Analysis of aftershocks duration

From equation (6), t_a is found to be inversely proportional to $\dot{\tau}$ when the parameter $A\sigma$ is kept constant (0.05 MPa) throughout the region. In our study region, t_a lies within the range 0–650 years. Figure 8 shows that the study region is predominantly occupied by low t_a values except some high values seen in Zone 5, which might be caused by longer stress relaxation times of the earthquakes occurred in this zone. Dieterich (1994) pointed out that t_a values range from 0.2 to 12 years for different regions worldwide; however, Toda et al. (2005) later calculated the values of t_a ranging between 5 and 500 years for constant $A\sigma$ (0.05 MPa). Catalli et al. (2008) estimated t_a values in between 5714.357 and 57143 years by considering constant $A\sigma$ (0.04 MPa) in the Umbria–Marche sector of Northern Apennines (Italy). Recently, Toda and Enescu (2011) have computed the t_a values within the range 0–100 years by assuming constant of $A\sigma$ (0.05 MPa) for Japan.

4.4. b-value variation

Figure 9 shows the spatial distribution of b-value in the study regime of Himalaya. The low b-value observed in the Kirthar ranges, nearby the eastern part of CF (Zone 1), can be correlated with the occurrences of large earthquakes, indicating high differential stress build-up in the zone. Higher b-values are found in the Hazara syntaxis of Northern Pakistan (Zone 2) suggesting an active ongoing creeping tectonics (Thingbaijam et al. 2009). However, low b-values are observed in Zones 3 and 4 that can be primarily associated with the presence of high differential stress accumulation within the rock mass. Moreover, high-stress pockets associated with low b-value arising out of the clustering events is observed along the southern part of Karakorum fault in the Tibetan Plateau region (Zone 5), which corroborates with findings of other researchers (Chingtham et al. 2015; Loannis et al. 2011; Shanker and Sharma 1998; Thingbaijam et al. 2009; Yadav et al. 2012).

4.5. Forecast model

The forecasted and the observed number of mainshocks having magnitude $M_W \geq 5$ during the years 2011–2013 are shown in Figure 10. The reference forecast model for the expected number of $M_W \geq 5$ mainshocks is prepared from the assumed $\Delta CFF = 0$ and average b-value (0.86) during the period 2011–2013 (Figure 10(a)). Figure 10(b) shows the expected number of $M_W \geq 5$ mainshocks estimated from the assumed $\Delta CFF = 0$ and spatially variable b-value during the period 2011–2013. However, Figure 10(c) depicts the forecasted frequency of $M_W \geq 5$ mainshocks, reproduced by considering average b-value (0.86) in our model, while stress perturbations and heterogeneous b-value are incorporated to predict the number of mainshocks with magnitude $M_W \geq 5$ in Figure 10(d). The expected number of $M_W \geq 5$ mainshocks estimated from the reference forecast model (Figure 10(a)) is more or less similar to the calculated seismicity rate r (Figure 7) due to the absence of stress perturbation (equations (2) and (3)). Figure 10(d) demonstrates that the forecasted seismicity rate is substantially well correlated

with the observed seismicity during the time period 2011–2013, whereas the forecast model incorporated with the constant ΔCFF and average b-value could not infer the observed seismicity, as shown in Figure 10(a)–(c).

Figure 10(d) clearly suggests that the forecasted seismicity is strongly influenced by ΔCFF and amplified background seismicity rate. However, the absence of observed mainshocks in high background seismicity rates can be primarily contributed to the shadow effect of ΔCFF. On the contrary, the forecast model also exhibits rather high seismicity in few areas of stress shadows. There are also some cases where model fails to explain observed seismicity rate increases, for example, in Zone 1. Such increase/decrease might be explained by dynamic Coulomb stress changes, which are sensitive to the direction of rupture propagation, local pore fluid effects and geothermal effect (Leptokaropoulos et al. 2014) or perhaps to locally anomalous rate/state parameters. Our forecasted seismicity rate could not explain the smaller changes due to small scale heterogeneities in ΔCFF. It is also noticed that the heterogeneity of spatial b-value increases the spatial heterogeneity of expected number of mainshock with magnitudes $M_W \geq 5$ (Figure 10(d)). Also, low b-value found in particular Kirthar ranges, Himalayan Frontal Thrusts and Tibetan Plateau region highlights the impact of the stress perturbation thereby increasing the production of expected number of lager mainshocks in the study region. More in-depth information regarding the effects of stress perturbation due to heterogeneous b-value can be obtained by simply examining Figures 9(d) and 10(b). However, the observed low b-value is solely responsible for high forecasted seismicity rate in southern Kirthar region of Zone1 and Tibetan plateau of Zone 5.

Toda and Stein (2003) affirmed that the high background seismicity along with long observational period is necessary to examine the stress shadows in the region. However, it is quite complicated to detect the small number of earthquakes occurred in the stress shadows from the maps depicting the forecasted number of mainshocks. This may be due to strong dependence of computed forecasted seismicity rate on the assumed stress history and input parameters that can vary over several orders of magnitude. For proper understanding of the absence of mainshocks in stress shadows, Figure 11 is presented by subtracting the expected numbers of $M_W \geq 5$ earthquakes prepared with the assumed ΔCFF = 0 from the ones with spatially variable stress perturbations. Furthermore, a careful observation indicates that the contribution of older events (29 July 1980 Nepal earthquake) to the seismicity is very less while the recent events, i.e. 7 April 2005 Xizang earthquake, 8 October 2005 Kashmir earthquake and 28 October 2008 Pakistan earthquake have remarkably increased the
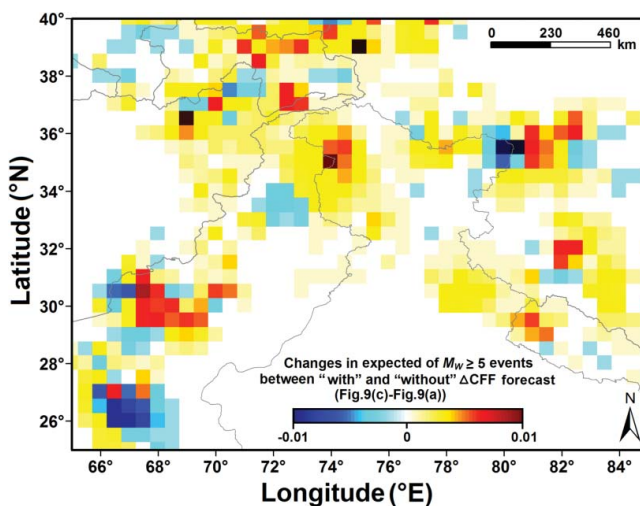

Figure 11. Expected number of $M_W \geq 5$ earthquakes after subtracting the matrix of Figure 10(b) from Figure 10(d) for investigating the effect of stress shadow in the study region. (To view this figure in colour, see the online version of the journal).
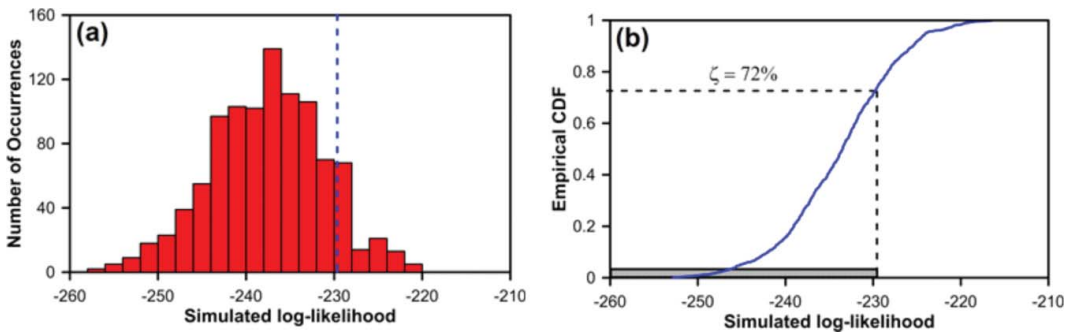
Figure 12. (a) Histogram of 1000 simulated joint log-likelihoods shown with observed joint log-likelihood (dashed blue line) estimated from the observed catalogue. (b) Empirical cumulative distribution for normalized S-test (solid blue line) simulated log-likelihoods along with the shaded critical region ($\alpha = 0.25\%$). (To view this figure in colour, see the online version of the journal).

seismicity. The stress shadows associated with the 17 June 1990 Pakistan earthquake, 20 May 1992 Pakistan earthquake and 27 February 1997 Pakistan earthquake (Figure 6) are scattered around the southern Kirthar ranges and Sulaiman ranges and thus the observed earthquakes in these areas are absent during the period 2011–2013.

Based on this static stress triggering, we find that the elastic stress transfer along with high r and low b-value promote seismicity rate changes consistent with the occurrence time and the location of the mainshocks. Our results agree with the main findings of Nostro et al. (2005) and Catalli et al. (2008) who calculated static stress changes for the 1997 Umbria–Marche sequence (central Italy) using rate/state friction model. Hence, the approach we adopted provides satisfactory results in forecasting the number of mainshocks with magnitudes $M_W \geq 5$ in the NW frontier province of Himalaya during the period 2011–2013 (Figure 10(d)). In summary, the forecast model applied in present study provides promising results, as it was able to forecast future seismicity rates, in spite of the aforementioned assumptions and uncertainties.

4.6. Consistency of the forecast model

In this study, we also attempt to assess the goodness-of-fit statistics for the forecast and the observed data (Figure 12). A histogram of 1000 simulated joint log-likelihoods along with observed data (dashed blue line) are plotted (Figure 12(a)). The intersection of the observed joint log-likelihood (dashed black line) with the corresponding empirical cumulative distribution functions of the simulated joint log-likelihoods (solid blue line) is also presented in (Figure 12(b)). It is apparent from these two figures that the quantile score ζ of S-test is found to be 72%, i.e. more than the critical region (shaded box) given by $\alpha = 2.5\%$. This implies that ζ lies outside the shaded critical region, thereby indicating the consistency of the spatial forecast and observed spatial distribution.

5. Conclusions

Coulomb stress transfer model incorporating rate and state dependent friction law is used in the study to forecast the seismicity rate of mainshocks with magnitudes $M_W \geq 5$ in the NW frontier of Himalaya during the period 2011–2013. For this purpose, we have computed ΔCFF, the most dominant parameter of the model, for each mainshock ($M_W \geq 5$) to examine the increase/decrease of seismicity rate due to stress perturbations. Also, other constituent parameters of this model such as smoothened background seismicity rate, aftershock duration,, and spatially variable b-value have been calculated for each source zone using compiled earthquake catalogue for the period 1975–2010. In this model, the heterogeneous b-value distribution tremendously increases the spatial heterogeneities of the forecasted mainshocks ($M_W \geq 5$) in the region. Although long observational periods

and high background seismicity rate before perturbing mainshocks are essentially required, the stress shadows associated with substantial seismicity rate are difficult to be detected because of sustained stress changes in the study region. The ΔCFF distributions that exhibit significant stress increase nearby the mainshock sources are found to be diminished with the inverse of the distance from the fault rupture plane, associated with the large mainshock. Despite of the presence of uncertainties in the model parameters and inadequate knowledge of dynamic stress triggering (i.e. propagation of seismic waves, postseismic slip and creeping, pore fluid diffusion, viscoelastic relaxation, and rheological properties), the rate and state transfer model captures the observed number of $M_W \geq 5$ mainshocks fairly well. The technique is found much better than that estimated using the stress changes alone. In addition, S-test has been performed to check the stability of the results, which confirm that the spatial distribution of forecasted and observed earthquakes match well. However, some mismatch between the observed and modelled seismicity rates may be associated because of additional uncertainties arising from the rate and state parameters, such as, aftershock duration, spatially uniform values of Aσ and the background seismicity rate.

However, the key aspects of the failure of forecasted seismicity rates map often depend on the poorly constrained parameters, whose values are chosen based on the preconceptions. In such case, forecasting of seismicity rates in any seismic regime will be poor. We can improve our model, if we choose the actual parameters based on the laboratory experimental value. Furthermore, recognizing the uncertainties would enable us to decide how much credence to place in the seismicity rates map and the forecast map should undergo rigorous and objective testing to compare their predictions to those of null hypotheses, including ones based on uniform regional seismicity.

Acknowledgements

Disclosure statement

No potential conflict of interest was reported by the authors.

References

Aki K. 1965. Maximum likelihood estimate of b in the formula log N = a – b. M and its confidence limits. Bull Earthq Res Inst. 43:237–239.

Avouac JP, Bollinger L, Lavé J, Cattin R, Flouzat M. 2001. Le cycle sismique en Himalaya. CR Acad Sci Paris, Sci de la Terre et des planètes/Earth and Planet Sci. 333:513–529. French.

Bapat A, Kulkarni RC, Guha SK. 1983. Catalogue of earthquakes in India and neighbourhood from historical period up to 1979. I.S.E.T. (Publ.); p. 1–211.

Bhloscaidh MN, Mccloskey J, Bean CJ. 2014. Response of the San Jacinto fault zone to static stress changes from the 1992 landers earthquake. J Geophys Res. 119:8914–8935. DOI:10.1002/2014JB011164.

Catalli F, Cocco M, Console R, Chiaraluce L. 2008. Modeling seismicity rate changes during the 1997 Umbria-Marche sequence (central Italy) through rate- and state-dependent model. J Geophys Res. 113:B11301. DOI:10.1029/2007JB005356.

Chandra U. 1978. Seismicity, earthquake mechanisms and tectonics along the Himalayan mountain range and vicinity. Phys Earth Planet Inter. 16:109–131.

Chingtham P, Chopra S, Baskoutas I, Bansal BK. 2014. An assessment of seismicity parameters in northwest Himalaya and adjoining regions. Nat Hazards. 71:1599–1616. DOI:10.1007/s11069-013-0967-5.

Chingtham P, Yadav RBS, Chopra S, Yadav AK, Gupta AK, Roy PNS. 2015. Time-dependent seismicity analysis in the Northwest Himalaya and its adjoining regions. Nat Hazards. 80(30);1783–1800. DOI:10.1007/s11069-015-2031-0.

Cocco M, Hainzl S, Catalli F, Enescu B, Lombardi AM, Woessner J. 2010. Sensitivity study of forecastedaftershock seismicity based on Coulomb stress calculation and rate-and state-dependent frictional response. J Geophys Res. 115:B05307. DOI:10.1029/2009JB006838.

Dieterich JH. 1979. Modeling of rock friction, 1, Experimental results and constitutive equations. J Geophys Res. 84:2161–2168.

Dieterich JH. 1994. A constitutive law for rate of earthquake production and its application to earthquake clustering. J Geophys Res. 99:2601–2618.

Fan G, Ni JF, Wallace TC. 1994. Active tectonics of the Pamirs and Karakorum. J Geophys Res. 99:7131–7160.

Frankel AD. 1995. Mapping seismic hazard in the central and eastern United States. Seismol Res Lett. 66:8–21.

Gomberg J, Beeler NM, Blanpied ML. 2000. On rate-state and Coulomb failure models. J Geophys Res. 105:7857–7872. DOI:10.1029/1999JB900438.

Gomberg J, Reasenberg P, Beeler NM, Cocco M, Belardinelli ME. 2005. A frictional population model of seismicity rate change. J Geophys Res. 110:B05S03. DOI:10.1029/2004JB003404.

Hainzl S, Enescu B, Cocco M, Woessner J, Catalli F, Wang R, Roth F. 2009. Aftershock modeling based on uncertain stress calculations. J Geophys Res. 114:B05309. DOI:10.1029/2008JB006011.

Hainzl S, Ogata Y. 2005. Detecting fluid signals in seismicity data through statistical earthquake modeling. J Geophys Res. 110:B05S07. DOI:10.1029/2004JB003247.

Hainzl S, Zoller G, Wang R. 2010. Impact of the receiver fault distribution on aftershock activity. J Geophys Res. 115:B05315. DOI:10.1029/2008JB006244.

Helmstetter A, Shaw BE. 2006. Relation between stress heterogeneityand aftershock rate in the rate-and-state model. J Geophys Res. 111:B07304. DOI:10.1029/2005JB004077.

Hintersberger E, Thiede RC, Strecker MR, Hacker BR. 2010. East–west extension in the NW Indian Himalaya. Geol Soc Am Bull. 122:1499–1515. DOI:10.1130/B26589.1.

Kagan YY, Jackson DD. 1995. New seismic gap hypothesis: Five years after. J Geophys Res. 100:3943–3959.

Khwaja AA, Monalisa. 2005. Seismic activity in the western extension of Salt Range. Pak J Meteorol. 2(3):35–47.

King GCP, Cocco M. 2001. Fault interaction by elastic stress changes: New clues from earthquake sequences. Adv Geophys. 44:1–39.

King GCP, Stein RS, Lin J. 1994. Static stress changes and the triggering of earthquakes. Bull Seismol Soc Am. 84:935–953.

Knopoff L. 2000. The magnitude distribution of declustered earthquakes in Southern California. Proc Natl Acad Sci U S A. 97:11880–11884. DOI:10.1073/pnas.190241297.

Leptokaropoulos K, Papadimitriou E, Orlecka-Sikora B, Karakostas V. 2014. Forecasting seismicity rates in western Turkey as inferred from earthquake catalogue and stressing history. Nat Hazards. 73:1817–1842. DOI:10.1007/s11069-014-1181-9.

Leptokaropoulos KM, Papadimitriou EE, Orlecka-Sikora B, Karakostas VG. 2012. Seismicity rate changes in association with the evolution of the stress field in northern Aegean Sea, Greece. Geophys J Int 188:1322–1338. DOI:10.1111/j.1365-246X.2011.05337.

Loannis B, George P, Chingtham P, Bansal BK. 2011. Temporal variation of seismic parameters in the western part of the India-Eurasia Plate Collision Zone. Res Geophys. 1:e3, 8–12.

Lombardi AM, Marzocchi W. 2007. Evidence of clustering and non-stationarity in the time distribution of large worldwide earthquakes. J Geophys Res. 112:B02303.

Lombardi AM, Marzocchi W, Selva J. 2006. Exploring the evolution of a volcanic seismic swarm: The case of the 2000 Izu Islands swarm. Geophys Res Lett. 33(7):L07310.

Mccloskey J, Nalbant SS, Steacy S. 2005. Earthquake risk from co-seismic stress. Nature. 434:291.

Nalbant SS, Hubert A, King GCP. 1998. Stress coupling between earthquakes in northwest Turkey and the north Aegean sea. J Geophys Res. 103:24469–24486.

Nalbant SS, Steacy S, Mccloskey J, Natawidjaja D. 2005. Earthquake risk on the Sunda trench. Nature. 435(7043):756–757.

Negi SS, Paul A, Cesca S, Kamal, Kriegerowski M, Mahesh P, Gupta S. 2017. Crustal velocity structure and earthquake processes of Garhwal-Kumaun Himalaya: Constraints from regional waveform inversion and array beam modeling. Tectonophysics. 712–713:45–63. DOI:10.1016/j.tecto.2017.05.007.

Nostro C, Chiaraluce L, Cocco M, Baumont D, Scotti O. 2005. Coulomb stress changes caused by repeated normal faulting earthquakes during the 1997 Umbria-Marche (central Italy) seismic sequence. J Geophys Res. 110:B05S20. DOI:10.1029/2004JB003386.

Ogata Y. 2005. Detection of anomalous seismicity as a stress change sensor. J Geophys Res. 110:B05S06. DOI:10.1029/2004JB003245.

Okada Y. 1992. Internal deformation due to shear and tensile faults in a half-space. Bull Seismol Soc Am. 82:1018–1040.

Oldham T. 1883. A catalogue of Indian earthquakes from the earliest time to the end of A.D. 1869. Mem Geol Surv India. 19(3):53.

Parsons T. 2002. Global Omori law decay of triggered earthquakes: large aftershocks outside the classical aftershock zone. J Geophys Res. 107(B9). DOI:10.1029/2001JB000646.

Parsons T, Yeats RS, Yagi Y, Hussain A. 2006. Static stress change from the 8 October, 2005 M 7.6 Kashmir earthquake. Geophys Res Lett. 33:L06304. DOI:10.1029/2005GL025429.

Philip G, Suresh N, Bhakuni SS. 2014. Active tectonics in the northwestern outer Himalaya: evidence of large-magnitude palaeoearthquakes in Pinjaur Dun and the frontal Himalaya. Current Sci. 106(2):211–222.

Schorlemmer D, Gerstenberger MC, Wiemer S, Jackson DD, Rhoades DA. 2007. Earthquake likelihood model testing. Seismol Res Lett. 78:17–29.

Shanker D, Paudyal H, Singh HN. 2011. Discourse on Seismotectonics of Nepal Himalaya and Vicinity: Appraisal to Earthquake Hazard. Geosciences. 1(1):1–15. DOI:10.5923/j.geo.20110101.01.

Shanker D, Sharma ML. 1998. Estimation of seismic hazard parameters for the Himalayas and its vicinity from complete data files. Pure Appl Geophys. 152:267–279.

Steacy S, Gomberg J, Cocco M. 2005. Introduction to special section: Stress transfer, earthquake triggering and time-dependent seismic hazard. J Geophys Res. 110:B05S01. DOI:10.1029/2005JB003692.

Stein RS. 1999. The role of stress transfer in earthquake occurrence. Nature. 402:605–609.

Stein RS. 2003. Earthquake conversations. Sci Am. 288:72–79.

Strader A, Jackson DD. 2015. Static Coulomb stress-based Southern California earthquake forecasts: A pseudoprospective test. J Geophys Res Solid Earth. 120:1667–1676. DOI:10.1002/2014JB011297.

Tandon AN, Srivastava HN. 1974. Earthquake occurrences in India. Meerut (India): Sarita Prakashan; p. 1–48.

Terakawa T, Matsu'ura M. 2008. CMT data inversion using a Bayesian information criterion to estimate seismogenic stress field. Geophys J Int. 172:674–685.

Thingbaijam KKS, Chingtham P, Nath, SK. 2009. Seismicity in the North-West Frontier province at the Indian-Eurasian Plate Convergence. Seismol Res Lett. 80(4):599–608.

Thingbaijam KKS, Nath SK, Yadav A. 2008. Recent seismicity in northeast India and its adjoining region. J Seismol. 12:107–123.

Toda S, Enescu B. 2011. Rate/state Coulomb stress transfer model for the CSEP Japan seismicity forecast. Earth Planets Space. 63:171–185.

Toda S, Stein RS. 2003. Toggling of seismicity by the 1997 Kagoshima earthquake couplet, A demonstration of time-dependent stress transfer. J Geophys Res. 108(B12):2567. DOI:10.1029/2003JB002527.

Toda S, Stein RS, Richards-Dinger K, Bozkurt SB. 2005. Forecasting the evolution of seismicity in southern California: Animations built on earthquake stress transfer. J Geophys Res. 110:B05S16. DOI:10.1029/2004JB003415.

Valdiya KS. 1991. Quaternary tectonic history of northwest Himalaya. Curr Sci. 61:664–668.

Wells DL, Coppersmith KJ. 1994. New empirical relationships among magnitude, rupture, length, rupture width, rupture area, and surface displacement. Bull Seismol Soc Am. 84:974–1002.

Yadav RBS, Bayrak Y, Tripathi JN, Chopra S, Singh AP, Bayrak E. 2011. A probabilistic assessment of earthquake hazard parameters in NW Himalaya and the adjoining region. Pure Appl Geophy. 169(9):1619–1639. DOI:10.1007/s00024-011-0434-8.

Yadav RBS, Tsapanos TM, Bayrak Y, Koravos CHG. 2012. Probabilistic appraisal of earthquake hazard parameters deduced from a Bayesian approach in the northwest frontier of the Himalayas. Pure Appl Geophys. 170(3):283–295.

Zechar JD, Gerstenberger MC, Rhoades DA. 2010. Likelihood-based tests for evaluating space–rate–magnitude earthquake forecasts. Bull Seismol Soc Am. 100(3):1184–1195.